Basement Membrane Mimetic Hydrogel Cooperates with ROCK Inhibitor to Promote the Development of Acini-Like Salivary Gland Spheroids

Eric W. Fowler, 1 Robert L	. Witt, ² and Xingiao.	Jia ^{1,3,4*}
----------------------------	-----------------------------------	-----------------------

¹Department of Materials Science and Engineering, University of Delaware, Newark, Delaware, 19716, USA

²Helen F. Graham Cancer Center and Research Institute, Christiana Care, Newark, Delaware, 19713, USA

³Department of Biomedical Engineering, University of Delaware, Newark, Delaware, 19716,

USA

⁴Delaware Biotechnology Institute, 590 Avenue 1743, Newark, DE 19713, USA

Keywords: Salivary Gland, Hyperbranched polyglycerol, Hyaluronic acid, Stem/progenitor cells, ROCK inhibitor.

Abstract

Successful engineering of functional salivary glands necessitates the creation of cellinstructive environments for ex vivo expansion and lineage specification of primary human salivary gland stem cells (hS/PCs). Herein, basement membrane mimetic hydrogels were prepared using hyaluronic acid, cell adhesive peptides, and hyperbranched polyglycerol (HPG), with or without sulfate groups, to produce "hyperGel+" or "hyperGel", respectively. Differential scanning fluorescence experiments confirmed the ability of the sulphated HPG precursor to stabilize fibroblast growth factor 10. The hydrogels were nanoporous, cytocompatibile and cell-permissive, enabling the development of multicellular hS/PC spheroids in 14 days. Incorporation of sulfated HPG species in the hydrogel enhanced cell proliferation. Culture of hS/PCs in hyperGel+ in the presence of a Rho kinase inhibitor, Y-27632 (Y-27), led to the development of spheroids with a central lumen, increased the expression of acinar marker aquaporin-3 at the transcript level (AQP3), and decreased the expression of ductal marker keratin 7 at both the transcript (KRT7) and the protein levels (K7). Reduced expression of transforming growth factor beta (TGF-β) targets SMAD2/3 was also observed in Y27-treated cultures, suggesting attenuation of TGF-β signaling. Thus, hyperGel+ cooperates with the ROCK inhibitor to promote the development of lumened spheroids with enhanced expression of acinar markers.

1. Introduction

Salivary glands produce saliva in response to a wide range of biochemical and environmental cues to maintain oral homeostasis.¹ The unique arrangement of acinar and ductal cells in this highly branched organ terminating in secretory end buds enables efficient vectorial transport of saliva.² Xerostomia (or dry mouth) occurs in patients with the autoimmune disease Sjögren's syndrome³⁻⁵ or subjected to standard radiotherapy for head and neck malignancies.⁶⁻⁸ Symptoms include severe dental issues, difficulties in swallowing, speaking, eating, gradual weight loss, and overall discomfort.⁹ Current clinical remedies for xerostomia aim to protect the salivary gland during radiation treatment, to palliate symptoms using water, oral sialagogues or anti-inflammatory agents, or to stimulate saliva secretion from the remaining salivary gland using cholinergic muscarinic receptor agonists. None has provided long-term therapeutic benefits.^{10, 11}

Tissue engineering offers regenerative opportunities for the treatment of salivary gland dysfunction. To this end, autologous human salivary gland stem/progenitor cells (hS/PCs) isolated from patients prior to radiation treatment are grown in a customized synthetic matrix to develop a secretory neotissue that can be implanted into the same host post radiation treatment. Successful engineering of functional salivary gland requires instructive and permissive matrices to facilitate the development of secretory constructs with a complex 3D tissue architecture. We have developed hyaluronic acid (HA)-based hydrogels that are conducive to the establishment of multicellular hS/PC spheroids, and identified the optimal matrix stiffness, protease degradability and peptide ligands that promote the rapid development of spheroids with enhanced expression of progenitor and acinar markers. Although our work represents a significant step forward towards the creation of tissue-engineered human salivary glands, a functional gland consisting of polarized acini remains to be realized.

The salivary gland epithelium is encased in the basement membrane, a thin, dense, nanoporous protein network comprised mainly of laminin, perlecan and collagen IV. The basement membrane defines the border between the epithelium and the surrounding stroma, provides structural support to the epithelium,^{21, 22} regulates growth factor diffusion and permeability, mediates cell signaling and cell motility, and plays crucial roles in the establishment of cell/cell junction and cell/tissue polarity.^{23, 24} As a heperan sulphate proteoglycan, perlecan sequesters and modulates growth factor activities by varying the sulphation pattern.^{21, 25, 26} During development, the basement membrane is actively modified and remodelled, through localized proteolytic degradation and global rearward translocation.² Alteration of the mechanical properties of the basement membrane profoundly influences cell and tissue shapes.²⁷ We hypothesize that 3D culture of hS/PCs in a synthetic matrix that incorporates key features of the native basement membrane will lead to the establishment of acini-like salivary gland spheroids.

We chose hyperbranched polyglycerol (HPG) as the starting material for the construction of basement membrane mimetic hydrogels. Hyperbranched polymers exhibit materials characteristics unachievable with traditional polymer architectures.^{28, 29} With the unique globular architecture, hyperbranched polymers display abundant functional groups and exhibit low intrinsic viscosity. Dendrimers are architecturally similar to hyperbranched polymers, but a multi-step iterative reaction sequence is required for the expansion of the core.²⁸ On the other hand, hyperbranched polymers can be readily synthesized via one-step polymerization methods, which can be readily scaled up. When an emulsifying agent is used, HPGs with molecular weights over 500,000 g/mol and narrow polydispersity index (PDI) are produced.³⁰ The ease of synthesis, combined with the unique materials properties, makes HPGs an ideal candidate for biomaterial applications. The multivalency afforded by high molecular weight HPG polymers allows the

incorporation of multiple biological signals useful in biomaterial applications. To date, HPG-based hydrogels were prepared using HPG polymers of low molecular weight (20,000 g/mol),³¹⁻⁴⁰ or broad PDL.⁴¹⁻⁴³

Here, hydrogels were prepared using thiolated hyaluronic acid (HA-SH) and acrylated HPG (HGP-AC). To promote integrin binding, fibronectin, and laminin-derived peptides, RGDSP and IKVAV, were conjugated to the network through thiolate-maleimide reaction. Additionally, a sulfated HPG crosslinker (HPG-AC-SO₃) was included to serve as synthetic analogues of heparan sulphate. The resultant hydrogels, with or without the sulphate moieties (hyperGel+ and hyperGel, respectively), were characterized compositionally, structurally, and mechanically. Both types of gels were conducive to the growth and expansion of hS/PCs. Using hyperGel+, we further explored the utility of a Rho-associated protein kinase (ROCK) inhibitor, Y-27632 (Y27), to promote the formation of lumened spheroids and to suppress ductal differentiation.

2. Materials and Methods

2.1. Materials.

Hyaluronic acid (HA, sodium salt, 430 kDa) was a generous gift from Sanofi Genzyme Corporation. All amino acids were purchased from Aapptec. Oxyma and N, N'-diisopropylcarbodiimide (DIC) were purchased from CEM and Chem Impex, respectively. Dialysis membranes (MWCO: 1 kDa) were purchased from Spectrum Labs. Reagents and chemicals used for the synthesis of HPG derivatives were procured from Fisher Scientific or Sigma Aldrich and used as received unless otherwise indicated.

2.2. Synthesis and Characterization of Hydrogel Precursors

2.1.1. Synthesis of hydrogel precursors.

HPG-OH. Under anhydrous conditions, trimethylolpropane (TMP, 1.39 mmol) was added to a 20% (w/v) potassium methylate (0.41 mmol) solution in methanol. After stirring for 30 min, methanol was removed under vacuum, the flask was purged with argon, and a mechanical stirrer was introduced. The reaction mixture was heated to 95 °C, and 25 mL of anhydrous dioxane was subsequently added. Glycidol (0.377 mol) was then added dropwise over 12 h using a syringe pump, and the reaction was maintained at 95 °C for additional 5 h. The reaction product was then dissolved in methanol and stirred over a cation-exchange resin (Amberlite IR120) for 2 h. The product was then precipitated twice in acetone. Finally, the polymer was dissolved in deionized water and dialyzed against deionized water for 72 h. The dry polymer was obtained by lyophilization.

HPG-AC. HPG-OH (0.5 g) and triethylamine (TEA, 0.68 mmol) were dissolved in 7.7 mL of anhydrous DMF and stirred over ice. A solution of acryloyl chloride (0.68 mmol) in 3.7 mL DMF was added dropwise, and the reaction was allowed to proceed overnight at room temperature. The solution was dialyzed against deionized water for 72 h. The purified product in deionized water was stored at -20 °C. Solution concentration and yield were determined by gravimetric analysis after lyophilization.

HPG-AC-SO₃. The HPG-OH/acryloyl chloride/TEA mixture was dialyzed against DMF, and dried thrice over activated 4 Å molecular sieves. To an anhydrous HPG-AC/DMF solution (5 mL) was added DMF–SO₃ complex (1.35 mmol, 1 M) in anhydrous DMF dropwise over 4 h at 60 °C. The mixture was stirred for additional 2 h at 60 °C, then maintained room temperature

overnight. The solution was dialyzed against deionized water for 72 h. The product, HPG-AC-SO₃, dissolved in deionized water, was stored at -20 °C. Solution concentration and yield were determined by gravimetric analysis of the lyophilized product.

<u>HA-SH.</u> HA-SH was prepared following our previously reported procedure. By ¹H NMR, percent thiolation was 65%. ⁴¹

Maleimide-functionalized cell adhesive peptides. MI-GGGRGDSPG (RGDSP-MI) and MI-GGGIKVAVSADR (IKVAV-MI) were synthesized at a 0.25 mmol scale using a Protein Technologies PS3 solid-phase peptide synthesizer, as previously described. ¹⁸ The product-specific m/z was confirmed with electrospray ionization (Xevo G2-S QTof), and purity was verified at 220/280 nm using a Shimadzu HPLC equipped with a Phenomenex C18 column.

2.2.2. Characterization of hydrogel precursors.

1H NMR. D₂O was added to the HPG/H₂O solution to a final volume ratio of H₂O/D₂O of 9/1 and spectra were recorded on a Bruker AV600 spectrometer applying a WATERGATE W5 pulse sequence.^{44, 45}

Gel permeation chromatography (GPC). The molecular weight and polydispersity of HPG derivatives were determined using a Waters 2695 GPC equipped with a Precision Instrument PD2100 SLS for simultaneous 15° and 90° scattering analysis. A mobile phase of 0.1 N NaNO3 was utilized at a 0.8 mL/min flow rate through two Ultrahydrogel 250 columns at 25 °C. The

reported dn/dc value for 0.1 N NaNO₃ was 0.12,⁴⁶ and refractive index measurements were made using a Waters 410 module.

Dilute solution viscosity. The viscosity of HPG-OH at 100, 75, 50, and 25 g/mL in 0.1 M NaNO₃ were measured at 25 °C using an Ubbelohde viscometer. Prior to measurement, the polymer solutions were filtered through a membrane with a pore size of 0.22 μ m. The intrinsic viscosity was determined from plots of reduced viscosity (η_{red}) and inherent viscosity (η_{inh}) against polymer concentration.

<u>Differential scanning fluorimetry (DSF)</u>. DSF was performed using an Applied Biosystems 7300 Real-Time PCR. PBS, fibroblast growth factor 10 (FGF10, Peprotech) in PBS, and HPG solutions mixed with Sypro Orange dye (Fisher Scientific) were added to an optically clear 96-well plate. The plate was then sealed with a clear adhesive film, and the samples were analyzed using thermal profile ramping in 1 °C/min increments from 25 °C to 95 °C.

<u>Dynamic light scattering (DLS)</u>. The hydrodynamic volume of the HPG derivatives was determined by DLS using a Malvern Zetasizer Nano ZS. Measurements were made in PBS at 25 °C at 1 mg/ mL.

Alcian blue assay. Following a reported method,⁴⁷ Alcian Blue 8GS (Fisher Scientific) was dissolved in deionized water containing 1.8 mM H₂SO₄ at 1 mg/mL. The solution was centrifuged at 12×g for 30 min and passed through a 0.22 μm filter. A working solution was prepared by mixing 0.25% (w/v) Triton X-100, 18.0 mM H₂SO₄, and 10% (w/v) stock dye solution. An equal

volume (10 μ L) of the HPG derivative in deionized water was mixed with a solution containing 27 mM H₂SO₄, 0.375% (w/v) Triton X-100, and 4.0 M guanidine HCl, before 100 μ L of the working dye solution was added. The mixture was centrifuged at 16×g for 10 min, and the resulting pellet was redissolved in 500 μ L of 8.0 M guanidine HCl. The solution was centrifuged again at 16×g for 3 min, and the supernatant (300 μ L) was added to a 96-well plate. The absorbance at 600 nm was recorded using SpectraMax® i3x multi-mode microplate reader.

2.3. Hydrogel Preparation and Characterization

2.3.1. Hydrogel synthesis.

Hydrogels were prepared by dissolving HA-SH at 1% (w/v) in sterile PBS with 5.55 mM glucose (PBS+), 0.6 mM RGDSP-MI and 0.3 mM IKVAV-MI. Separately, HPG-AC and HPG-AC-SO₃ were prepared at 1% (w/v) in PBS+ and sterilized by filtration through a 0.22 μm membrane. After the pH of the HA/peptide solution was adjusted to 7.4 using 1 M NaOH, the HPG-AC solution was added at a 1/3 (v/v) ratio to produce the hyperGel. HyperGel+ was prepared using an HPG-AC solution containing 5% (v/v) HPG-AC-SO₃. In both cases, the HPG solution was combined with the HA/peptide solution at a volume ration of 1/3 (Table 1).

Table 1: Formulations of hyperGel and hyperGel+.

	HA-SH (mg/mL)	RGD-MI (mM)	IKVAV-MI (mM)	HPG-AC (mg/mL)	HPG-AC-SO ₃ (mg/mL)
HyperGel	6.67	0.5	0.1	6.67	
HyperGel+	6.67	0.5	0.1	6.33	0.33

2.3.2. Hydrogel characterization

Oscillatory rheology. Hydrogel viscoelasticity was evaluated using a controlled stress rheometer (AR-G2, TA Instruments) with a 20 mm parallel plate geometry at 25 °C. After loading the hydrogel precursor mixture on the bottom plate, the top plate was lowered to maintain a 100-µm gap. Mineral oil was applied around the geometry to prevent evaporation. Time sweep was performed at 1.0 % strain and 1.0 Hz for 2 h. Frequency sweep was conducted at 1% strain at 0.01 to 10 Hz, while strain sweep was implemented from 0.1 to 1000% strain at 1.0 Hz. The storage (G') and loss (G") moduli were reported as the average of experiments conducted in triplicate.

Alcian blue staining. Alcian Blue 8GS was dissolved at 10 mg/mL in deionized water with 3% (v/v) glacial acetic (pH 2.5) and passed through a 0.22 μ m filter. After the hydrogels (30 μ L) were equilibrated in PBS for 24 h, the staining solution was added, and samples were incubated at ambient temperature for 15 min. The gels were washed with water three times (5 min each) before digital images were captured.

Fluorescence recovery after photobleaching (FRAP). HPG crosslinkers and HA-SH were prepared in PBS solutions containing 0.6 mg/mL FITC-dextran (40, 150, 250, or 500 kDa, Fisher Scientific). Gels (30 μL) were prepared in 35 mm MatTek glass-bottom Petri dishes and equilibrated in 1.5 mL of 0.6 mg/mL FITC-dextran PBS solutions for 72 h at room temperature with gentle shaking. FRAP was conducted using Zeiss 880 LSM equipped with a 40× objective, 32 μm pinhole, and 488 nm argon laser. Measurements were made from the coverslip 30 μm into the hydrogel and the results were captured as 512×512-pixel images. Fifteen pre-bleach images were recorded before a circle with a 51.82 μm radius was bleached to 30% of the pre-bleach intensity within 10 s. Fluorescence recovery was monitored every ~0.6 s for a total of 500 images

at 0.2 % laser power. Fluorescent recovery profiles were analyzed using OriginLab's non-linear squares regression to fit the Soumpasis equation (1): where f(t) is normalized recovered fluorescent intensity, t represents time, τ_D is characteristic diffusion time, k is the mobile fraction, and I_0 and I_1 are modified Bessel functions of the first kind.⁴⁸

$$f(t) = k * e^{-\frac{\tau_D}{2t} \left[I_0 \left(\frac{\tau_D}{2t} \right) + I_1 \left(\frac{\tau_D}{2t} \right) \right]}$$
 (1)

The lateral 2D diffusivity was calculated from equation (2): where D is the effective and ω represents the bleach spot radius.⁴⁹ Dextran radius of hydration was taken as the manufacturer's reported value and estimated from literature values when not supplied.⁵⁰

$$D = \frac{\omega^2}{\tau_D} \tag{2}$$

2.4. Development of Multicellular hS/PC Spheroids

2.4.1. Cell maintenance. Following previously reported methods, ¹⁷ hS/PCs were isolated from human parotid gland tissues from consenting patients with approval from Christiana Care and the University of Delaware. Cells were maintained in HepatoSTIM media (Corning) to 70-80% confluence and trypsinized with 0.05% (w/v) trypsin-EDTA, which was neutralized with a trypsin soybean inhibitor.

2.4.2. 3D cell encapsulation. HA/peptide solution containing suspended hS/PCs at pH 7.4 was mixed with the HPG crosslinker (Table 1) to afford a cellular construct with 1×10^6 cells/mL. The gelling liquid (30 μ L) was transferred to well in a 48-well glass bottom MatTek plate and incubated at 37 °C for 20 min before adding 500 μ L of Hepato-STIM medium. For qPCR analysis,

a larger construct was prepared in a 12-mm cell culture insert with 100 μ L gel mixture, and additional 800 μ L of Hepato-STIM medium was added for 3D culture.

2.4.3. Viability and proliferation. After 1, 7, and 14 days of culture, the cellular construct was rinsed with PBS and incubated in a solution containing Calcein AM (4 μM, Thermo Fisher Scientific), ethidium homodimer (EthD-1, 4 μM, Thermo Fisher Scientific), and Hoechst 33342 (4 μM, Life Technologies) for 15 min at 37 °C. The solution was then aspirated, the construct was washed twice with PBS, and images were acquired with a Zeiss LSM 710 confocal microscope. Using ImageJ, viability was quantified as a percentage of EthD-1 positive nuclei over the total Hoechst 33324-stained nuclei. Proliferation was estimated by the ratio of Hoechst positive nuclei on day 1 compared to the Hoechst positive nuclei on days 3, 7, and 14 of culture.

2.4.4. Cell morphology. Constructs were fixed with 4% paraformaldehyde (PFA, Sigma Aldrich) in PBS for 30 min at room temperature, washed with PBS three times (10 min each), permeabilized with 0.1% Triton for 30 min and blocked with 3% (w/v) bovine serum albumin (BSA) overnight at room temperature. Samples were then incubated with Alexa Fluor 568 Phalloidin (1:400 dilution, Life Technologies) for 16 h at room temperature, followed by three PBS washes (10 min each). Next, samples were incubated with 4',6-diamidino-2-phenylindole (DAPI, Life Technologies) at 1:500 dilution in PBS for 30 min at room temperature. Three PBS washes were performed (10 min each), and confocal imaging was performed using a Zeiss LSM 880 equipped with an Airyscan detector in Fast Airyscan mode. Images were captured as z-stacks of 101.18 μm and maximum intensity projection was performed. Feret's diameter and circularity were quantified with ImageJ.

- 2.4.5. Immunofluorescence. The cell-laden hydrogels were fixed with 4% PFA for 30 min, blocked with 3% (w/v) BSA in PBS containing 0.2% Triton (PBST) for 16 h at room temperature. Constructs were incubated with a primary antibody against SMAD2/3 (Cell Signaling Technology) that was diluted in PBST with 3% (w/v) BSA at 1/100 for 48 h at room temperature, washed with PBST three times (15 min each), and incubated in PBST for an additional 16 h. Constructs were subsequently incubated with Alexa Fluor-488 AffiniPure Fab Fragment antirabbit secondary antibody (Jackson Immunoresearch Labs) diluted 1/200 in PBST with 3% BSA for 48 h at room temperature. Constructs were washed three times with PBST (15 min each), counterstained with DAPI (1/500 in PBST) for 30 min and imaged using a Zeiss LSM 880 equipped with an Airyscan detector in Fast Airyscan mode.
- **2.4.6.** Gene expression. Cellular constructs were snap-frozen in dry ice/isopropanol, and total RNA was extracted using Trizol (Invitrogen). Subsequently, reverse transcription was performed using the QuantiTect Reverse Transcription Kit (QIAGEN). The resulting cDNA was prepared with primers and Power SYBR green master mix before qPCR was performed using an ABI 7300 real-time PCR system. Glyceraldehyde 3-phosphate dehydrogenase (GAPDH) and peptidylprolyl isomerase A (PPIA) were utilized as reference targets. The fold change was assessed with qbase+ software (Biogazelle). A total of three biological repeats were analyzed for each hydrogel composition.
- **2.4.7. Western blotting.** Protein lysate was extracted via Trizol and the protein concentration was quantified using a Micro BCA Protein Assay Kit (Thermo Scientific) using a

SpectraMax i3x Multi-Mode Microplate Reader. Samples were run on a 4-20% Mini-PROTEAN Gel before transferring to a nitrocellulose membrane. Revert 700 Total Protein Stain was used for lane normalization. Membranes were blocked with 5% (w/v) skim milk in 0.1 Tween 20 tris buffered saline (TBST) for 2 hr at room temperature. Anti-keratin-7 (Thermo Scientific) was diluted in blocking buffer 1/200 and incubated for 16 h at 4 °C. Samples were washed with TBST 3 times for 5 min. Membranes were incubated with alkaline phosphatase-linked anti-mouse antibody (Cell Signaling Technology) diluted in blocking buffer (1/20,000) for 1 h at room temperature. Membranes were treated with Amersham ECF substrate (Millipore Sigma) and images were captured using an iBright FL1500 Imaging System. Blots were analyzed using ImageJ.

2.4.8. Statistical Analysis. Statistical comparisons between two groups were carried out using a two-tailed Student's t-test. When comparing more than two groups an analysis of variance (ANOVA) was performed, and when applicable, a post-hoc Tukey multiple comparisons test was carried out. A p value < 0.05 was deemed significant. Statistical interpretations were made using JMP Pro 15 (SAS Institute Inc.).

3. Results and Discussion

3.1. Preparation of multifunctional hyperbranched crosslinkers

Solvent-assisted ring-opening multibranching polymerization (ROMBP)³⁰ was employed to synthesize HPG-OH from monomeric glycidol (Figure 1A). The idealized structure of HPG-OH (Figure 1B), containing linear, dendritic, and terminal units, was confirmed by inverse-gated ¹³C-NMR, with an estimated degree of branching of 0.51 (Figure S1). An intrinsic viscosity of

4.05 mL/g, consistent with that of previously reported HPGs,^{28, 46} further indicated the compact branched architecture of these polymers (Figure S2). ¹H-NMR analysis indicated the presence of hydroxyl groups at 5.0-5.75 ppm with the representative glycidol backbone protons at 3.2-4.2 ppm (CH₂-CHOR-CH₂OR, Figure 1C). Use of dioxane as an emulsifying agent^{29, 30, 46} enabled the synthesis of HPG-OH with a very high molecular weight, with M_n over 600,000 g/mol, and a narrow PDI (Table 2). To synthesize a multifunctional crosslinker that participates in Michael addition reaction with thiolated HA (HA-SH) as the Michael acceptor, acrylate groups were installed through the reaction of linear and dendritic hydroxyls with acryloyl chloride (Figure 1A). Acryloyl chloride was chosen to avoid the possibility of hydrophobic reaction by-products being trapped in the hyperbranched polymer.⁵¹⁻⁵³ To ensure high water solubility of the product, only 10% of hydroxyls were targeted for modification.

Table 2. Characterization of HPG-OH and HPG-AC by GPC and dilution solution viscometry.

	M _w (g/mol)	$M_n(g/mol)$	PDI	η (mL/g)
HPG-OH	657,000	587,200	1.12	4.05
HPG-AC	725,300	630,100	1.15	

 M_w : weight average molecular weight; M_n : number average molecular weight; PDI: polydispersity index; η : intrinsic viscosity.

Successful acrylation was confirmed by $^1\text{H-NMR}$ by the appearance of the characteristic vinyl proton peaks at 6.0-6.5 ppm ($^-\text{CH=-CH}_2$). Peak integration and normalization to the glycidol backbone protons indicated 9 \pm 1% acrylation (Figure 1C). Characterization with GPC-MALS indicated successful acrylate functionalization (Table 2, Figure 1D). The unmodified HPG-OH was synthesized at a M_n of 5.87×10^5 g/mol with a PDI of 1.12. After acrylation, M_n increased to 6.3×10^5 g/mol while the PDI only modestly broadened.

High molecular weight HPG-OH developed here have nearly 8,000 hydroxyl groups that can be utilized to incorporate multiple functionalities of the basement membrane. We are interested in recapitulating the ability of perlecan to sequester growth factors through the sulphated glycosaminoglycan (GAG) side chains. Thus, the remaining OH groups on HPG-AC were converted to sulfate moieties by reaction with the sulfur trioxide-DMF complex. A significant decrease in signal intensity for hydroxyl protons at 5.0-5.75 ppm suggested successful sulfation, while the acrylate functionality was retained at $\sim 9 \pm 1\%$ (Figure 1C). The product, HGP-AC-SO₃, can be used for crosslinking purposes to stably conjugate the sulfate moieties to a hydrogel network for binding and association with proteins via multivalent charge interactions.

Characterization of HPG derivatives by dynamic light scattering (DLS) further confirmed successful chemical transformations (Figure 1E). A hydrodynamic diameter (Dh) of 15.9 ± 0.1 nm for HPG-OH was similar to published values for low PDI, high molecular weight hyperbranched polyglycerols.^{29, 30, 46} The unimodal distribution of polymeric species indicates the absence of polymer aggregation. After acrylation, Dh increased significantly (p = 0.0001, Figure S3A) to 16.8 ± 0.1 nm, consistent with the increase in molecular weight. After sulfation, Dh decreased significantly (p = 0.0001, Figure S3A) to 15.3 ± 0.1 nm. The hydrodynamic diameter of HPG-AC-SO₃ was independent of pH (3-10) and was consistently smaller than that for HPG-AC (Figure S3B). The acidic conditions employed for sulfation may lead to intramolecular condensation and partial hydrolysis of the ester group linking the unsaturated double bond to the HPG backbone.⁵⁴

To further confirm the presence of sulfate groups in HPG-AC-SO₃, Alcian blue assay⁴⁷ was performed (Figure 2A). As the amount of HPG-AC-SO₃ increased from 3.1 µg to 100 µg, the absorbance at 600 nm, characteristic of the dye-sulphate complex,⁴⁷ increased linearly indicating that the increased absorbance was due to the dye complexing with the sulfate groups in HPG-AC-

SO₃. Because HPG-OH is highly non-fouling,^{55, 56} non-specific physical association of the dye with the polymer backbone is unlikely. HPG-AC did not bind Alcian Blue, further confirming that the sulfate groups on HPG-AC-SO₃ were responsible for binding. Although HA is negatively charged, it is not sulphated, and as expected, could not bind Alcian Bluein this assay.

GAGs have been reported to regulate salivary gland branching morphogenesis by patterning fibroblast growth factor-10 (FGF10) activity across the basement membrane. ^{26, 57} We hypothesized that sulfated hyperbranched polymers could synthetically recapitulate the function of GAGs. Here, differential scanning fluorimetry (DSF) was employed to ascertain the ability of HPG-AC-SO₃ to bind and stabilized the denature-prone FGF10 (Figure 2B). Upon binding to hydrophobic regions of denatured FGF10, the fluorescence intensity of Sypro Orange dye is significantly enhanced, and therefore can be used to detect protein unfolding. FGF10 is exceptionally unstable, 58 degrading in cell culture conditions within 30 min. 59 Thus, FGF10 is a good candidate to assess protein stabilization imparted by HPG-AC-SO₃. DSF analysis indicated a melting temperature of 43 °C for FGF10 when loaded with the vehicle PBS, in agreement with literature values. 58,59 When FGF10 was combined with HPG-AC-SO3, the sulfated HPG acted as a scaffold to thermally stabilize the three-dimensional structure of FGF10, increasing the melting temperature to 51 °C. Contrarily, the DSF trace for HPG-AC/FGF10 overlaps perfectly with that for PBS/FGF10, indicating minimal interactions between HGP-AC and FGF10. Collectively, high molecular weight, monodisperse HPG-OH was successfully synthesized under well-defined conditions. Post polymerization modification through the hydroxyls led to successful installation of the Michael acceptor (the acrylate group) for covalent crosslinking purposes and the sulfate groups for growth factor sequestration and stabilization. These chemical modifications did not compromise the branched molecular architecture.

3.2. Establishment of basement membrane mimetic hydrogels.

HPG-AC was mixed with HA-SH to produce hyperGel via Michael type addition reaction (Figure 3A). The modular hydrogel design allowed the incorporation of HPG-AC-SO₃ by combining with HPG-AC at a 5/95 v/v ratio to produce the sulfate-decorated hyperGel+ (Figure 3B). Including the HPG-AC-SO₃ species did not deteriorate gel formation, and the hydrogels maintained a disk shape (Figure 3C). Gels prepared without HPG-AC-SO₃ were stained lightly blue by Alcian blue at pH 3.5 due to the backbone charge of HA-SH. Hydrogels prepared with HPG-AC-SO₃ were stained intensely blue, confirming the presence of sulfated species in hyperGel+.

Upon mixing, the reaction between HPG-AC and HA-SH resulted in network formation within 5 min, as indicated by the crossover point when G' = G'' in the time sweep experiment (Figure 3D). Two hours later, G' and $tan(\delta)$ of the hyperGel reached 25.8 ± 2.4 Pa, and 0.01 ± 0.01 , respectively, indicating the formation of a viscoelastic gel. Though exceptionally soft, G' and G'' values were not frequency-dependent, indicating the formation of a stably covalently crosslinked hydrogel. Rheological analysis of water-swollen hyperGel showed a moderate increase in G' (57.6 \pm 10.4 Pa, Figure S4) compared to the as synthesized hyperGel, potentially due to additional slow crosslinking occurring as the buried hyperbranched acrylates were revealed by swelling. The average G' value for fully swollen hyperGel+ was determined as 74.2 \pm 15.0 Pa, which was not significantly (p = 0.4) different from that for the hyperGel. Therefore, the addition of 5% HPG-AC-SO₃ did alter the gel stiffness.

We have previously demonstrated that compliant hydrogels with a G' of 35-216 Pa promote the 3D assembly of hS/PC spheroids. These previously reported hydrogels were prepared by combining HA-SH with a linear, low molecular weight HA with 50% acrylate

incorporation (HA-AC). Replacing HA-AC with the HPG-AC ensured the generation of cell permissible hydrogels with a relatively low stiffness while maintaining rapid gelation due to the hyperbranched molecular architecture (Figure 3B). When covalently integrated in a network, the unreacted branches of the HPG building blocks serve as non-elastically active chains, reducing the overall crosslinking density.

To evaluate solute mobility within the hyperGel network, fluorescence recovery after photobleaching (FRAP) was performed using FITC-dextran probes of varying molecular weights (Figure 4A). The smallest probe with a molecular weight of 40 kDa rapidly recovered fluorescence at the bleached region in 40 s, while the 150 kDa probe demonstrated a slower recovery response (Figure 4A, B). As the molecular weight increased above 150 kDa, the rate of fluorescence recovery decreased substantially. The diffusion coefficient of FITC-dextran probes in the hyperGel (Dg) was determined by fitting the Soumpasis equation to the recovery plots for each probe. As expected, larger probes diffused more slowly (Figure S5).

The unique structure of the hyperGel was revealed by normalizing D_g to D_o, the diffusion coefficient of the probe molecules in the swelling medium (PBS). As the molecular weight of FITC-dextran increased from 150 kDa (D_h: 17.90 nm) to 500 kDa (D_h: 31.80 nm), the D_g/D_o value progressively decreased (Figure 4C). On the other hand, as the molecular weight decreased from 150 kDa to 40 kDa (D_h: 8.94 nm), the D_g/D_o value also decreased. Thus, the 40 kDa FITC-dextran diffused 50% slower in the hyperGel than in PBS. We anticipate that the small 40 kDa probe can penetrate the core of the hyperbranched structure, interact with the HPG units, and follow a more tortuous path as it diffuses through the network. Consequently, the normalized diffusion coefficient is low. Contrarily, the larger 150 kDa probe avoided the hyperbranched nanostructure and move freely through the pores of the bulk gel, thereby exhibiting a higher D_g/D_o value. As the

molecular weight of the probe increases to 500 kDa, its diffusion is significantly restricted by the bulk gel porosity, thus exhibiting a lower D_g/D_o value.

The encapsulation and retention of nanoparticles was used to estimate the bulk hyperGel pore size. In the diameter range from 35 to 100 nm, the hyperGel exhibited high particle retention. No significant differences in nanoparticle retention were detected in this size range (Figure 4D). The inability of the 35 nm particle to diffuse through the network suggests that the network exhibits an average pore size less than 35 nm, which agrees with the FRAP analysis.

The salivary gland epithelium is surrounded by a dense protein network (the basement membrane) that regulates tissue development and homeostasis.^{2, 21} As a nanoporous scaffold, the basement membrane essentially act as a filtration membrane, controlling growth factor and cytokine permeability.³⁸ The hyperbranched architecture of HPG crosslinkers enabled the establishment a dense, nonporous scaffold that is mechanically compliant, similar to the native basement membrane. Our findings are in agreement with previous reports, where HPG crosslinkers were shown to be more restrictive to diffusion than linear bis-functional polyethylene glycol (PEG) crosslinkers.³¹

3.3. 3D growth of hS/PCs in hyperGel+.

For 3D culture, hS/PCs were first dispersed as single cells in PBS containing HA-SH, RGD-MI and IKVAV-MI. Cellular constructs were established upon addition of HPG crosslinkers (HPG-AC or HPG-AC/HPG-AC-SO₃) at pH 7.4. The custom hyperGel supported the development of multicellular structures. By day 14, spheroids with an average diameter greater than 70 μ m were observed (Figure 5A). Viability was maintained at 81.0 \pm 1.0 % on day 1 and increased to 91 \pm 1.0 %, and 96 \pm 1.0 % on day 7 and day 14, respectively (Figure 5B). A comparable level of viability

was observed between hyperGel and hyperGel+ constructs. The lower viability on day 1 may be due to cellular stress introduced during encapsulation. Overall, the hyperGels and its constituent building blocks are cytocompatible with hS/PCs.

The hyperGels supported the 3D expansion of hS/PCs. Over the initial 7 days of culture, hS/PCs proliferated by 2.74 ± 0.23 folds. Cell proliferation increased further on day 14 to 3.57 ± 0.31 -fold (Figure 5C). When sulfated species were incorporated in the network, cell proliferation was increased by 2.91 ± 0.36 and 4.95 ± 0.72 folds on day 7 and day 14, respectively. Cell proliferation on day 14 in hyperGel+ was significantly (p < 0.05) higher than in the sulfate free hyperGel controls. The volume of the multicellular structures, as Calcein+ volume, was further analyzed based on 3D renderings of confocal images. While no differences were observed between the two gel formulations on day 7, with continued culture, proliferation was sustained in the hyperGel+ to day 14 which resulted in significantly (p < 0.05) more Calcein+ volume than in the hyperGel on day 14 (Figure 5D).

For 3D assembly of salivary gland spheroids, the encapsulated hS/PCs must interact with the extracellular matrix and growth factors. Our previous work showed that incorporation of integrin binding peptide, RGDSP (0.25 mM), in covalently crosslinked HA gels promoted the rapid development of multicellular spheroids. On the other hand, introduction of a laminin derived peptide, IKVAV (1 mM), effectively maintained the stem/progenitor status. ¹⁸ Thus, RGDSP and IKVAV signals were included in the hydrogel formulations investigated here. During development, many organ-specific growth factors cooperatively guide the epithelial cell to undergo growth, proliferation, differentiation, migration, and apoptosis to establish the branched tissue architecture. Importantly, the activity of various growth factors, such as those belonging to the fibroblast growth factor (FGF), transforming growth factor (TGF), bone morphogenetic protein

(BMP) and epidermal growth factor (EGF) superfamilies, is regulated by heparan sulphates in the basement membrane and on cell surfaces, though the interactions of growth factors with the sulfated side-chains of heparan sulphate proteoglycans.¹⁷ The superior performance of hyperGel+ over the sulfate free hyperGel can be attributed to the ability of the sulfate groups to sequester and stabilized growth factors secreted by cells, thereby enhancing their bioavailability to hS/PCs.

3.4. Supplementation of 3D cultures with Y-27.

For the treatment of radiation induced xerostomia, tissue engineered constructs should contain organized cell assemblies consisted of pracinar progenitor cells. Studies have shown that, during development, Rho-kinases (ROCK) play an important role in cleft formation and basement membrane positioning in epithelial tissue polarity. ^{60,61} However, in cell cultures, ROCK activation can lead to cell apoptosis and cell plasticity (acinar to ductal transformation). ⁶² Therefore, to maximize the regenerative potential of hS/PCs, hS/PCs were cultivated in hyperGel+ in the presence of a ROCK inhibitor, Y-27632 (Y27). In our experiments, hS/PCs were encapsulated as single cells in the hyperGel+, and Y27 was supplemented in the medium on day 3. Y-27 did not significantly alter cell proliferation as compared to the vehicle control samples (PBS) after 14 days of culture (Figure 6A, C).

Spheroid morphology was assessed with confocal microscopy after F-actin and DAPI staining (Figure 6B, D). Quantification by ImageJ indicated that Y27 treatment led to the establishment of significantly (p < 0.05) larger spheroids (Figure 6E). Spheroids established in the control cultures were compact and rarely contained a lumen. Spheroid surface was smooth and cortical F-actin was detected at the border of the spheroids and between neighbouring cells. On the other hand, spheroids developed in Y27 treated cultures contained a central lumen surrounded

by a single layer of epithelial cells with elongated nuclei in ~56% of the spheroids while only ~0.03% spheroids developed under control conditions exhibited a lumen. Y27 treated cultures also exhibited a significantly reduced variance in the nuclear distance from the spheroid centroid, indicating formation of highly organized structures. Y27 is reported to reduce cortical actin tension, ⁶³ and this could allow the nuclei to become more organized.

Salivary gland epithelium must maintain apicobasal polarization to achieve proper unidirectional secretion of saliva. ^{64,65} In Y-27 treated cultures, we observed F-actin-rich filopodia (arrow in Figure 6D) lining the apical surface of the spheroids and additional F-actin-rich structures (arrowhead, Figure 6D) protruding into the surrounding hydrogel. The strong F-actin staining along the apical domain is a hallmark of lumen formation and is frequently observed in polarized epithelial structures. ⁶⁶⁻⁶⁸ In line with our observations, previous work showed that excess ROCK-driven actomyosin contractility resulted in disturbed epithelial polarity and cystogenesis, and pharmacological inhibition of ROCK rescued the formation of polarized cysts. ⁶⁹ Because myosin II is a major downstream effector of ROCK, Y-27 treatment led to reduced myosin II activity at the cortical F-actin barrier, permitting the outgrowth of F-actin protrusions as observed in Caco-2 and SK-CO15 cells. ^{70,71} The unique F-actin structures seen upon ROCK inhibition might attributed to hyperGel+ matrix that is soft, but non-degradable.

qPCR experiments were performed on day 14 hyperGel+ constructs for genes encoding salivary gland differentiation markers (Figure 7A). Keratin-5 (*KRT5*), keratin-14 (*KRT14*), and the transcription factor transformation-related protein 63 (*TP63*) expressed by salivary gland basal/stem cells^{72, 73} were differentially regulated under the experimental conditions employed. Compared to the PBS controls, Y-27 cultures expressed a significantly higher level of *TP63* (2.0 \pm 0.24 folds, p < 0.002). Characterization of genes expressed by ductal salivary gland cells,

including keratin-7 (*KRT7*), keratin-8 (*KRT8*) and keratin-18 (*KRT18*), showed *KRT7* expression was specifically downregulated (> 3-fold, p < 0.001) in response to Y27 treatment. We further characterized the expression of acinar marker⁷² aquaporin-3 (*AQP3*) and observed a significant enhancement in its expression in Y-27 cultures (2.41 \pm 0.27 folds, p < 0.001). The increased expression of *TP63* and *AQP3*, along with the decreased expression of *KRT7* suggests that Y27 promotes a proacinar progenitor phenotype.

We have recently reported that RGD-mediated TGF-β1 signaling in synthetic HA hydrogels can promote the expression *KRT7*/K7. K7 is a ductal marker and an indicator of cellular stress. Inhibition of TGF-β signaling supports the proliferation of primary p63 positive salivary gland cells.⁷⁴ Here, we assessed whether Y27 decreased TGF-β1 signaling in hS/PCs cultured in the hyperGel+. Analysis by Western blotting indicated approximately 2-fold decrease in K7 expression with Y27 treatment (Figure 7B, Figure S6), confirming the downregulation of K7 at the protein level. We next investigated if the down regulation of K7 was due to reduced TGF-β signaling. Characterization of the expression of SMAD2/3, downstream effectors of TGF-β1 signaling, showed that both nuclear and cytoplasmic levels of SMAD2/3 were reduced with Y27 treatment (Figure 7E, D), although the nuclear/cytoplasmic ratio was unchanged (Figure 7F). These findings suggest that Y-27 reduced TGF-β signaling and promoted the expression of genes involved with progenitor identity.

Collectively, our results confirmed the utility hyperGel+ as a basement membrane mimetic scaffold for 3D culture of hS/PCs. Quantification of growth factors secreted by the resident hS/PCs and analysis of cytoskeleton remodelling in response to Y-27 will likely shed light into how hyperGel+ promoted the rapid development of epithelial spheroids and how Y-27 induced the formation of acini-like structures with a common lumen. In our studies, RGDSP and IKVAV

peptides were separately coupled to the HA chains. The high degree of functionality offered by HPG permits direct conjugation of thousands of copies of peptides to a single polymer to afford a multifunctional molecular construct that recaptures the key cell-modulating motifs in the native basement membrane for an enhanced biological response. Finally, co-culture of hS/PCs with mesenchymal cells in hyperGel+ can improve the utility of adult salivary stem/progenitor cells in salivary gland tissue engineering.

4. Conclusion

High molecular weight, monodisperse hyperbranched polyglycerol conjugates carrying acrylate and sulfate moieties were synthesized and characterized. Combining the hyperbranched building blocks with thiolated HA and cell adhesive peptides resulted in the establishment of cell permissive hydrogels suitable for 3D culture of hS/PCs. With the unique nanoporous structure and the presence of sulfate moieties and laminin motifs, the hyperGel+ resembles the native basement membrane surrounding the native gland. hyperGel+ permitted the establishment of multicellular hS/PC spheroids. Supplementation of culture media with Y27 accelerated cell growth, promoted acinar differentiation, promoted the development of polarized lumen, at the same time, ameliorating the undesirable TGF-β signaling associated with cellular stress.

Author Information

Corresponding Author: Xinqiao Jia, Department of Materials Science and Engineering, Department of Biomedical Engineering, Delaware Biotechnology Institute, University of Delaware, Newark, Delaware, 19716, USA. E-mail: xjia@udel.edu

Author Contributions: The manuscript was written through contributions of all authors. All authors have given approval to the final version of the manuscript.

Acknowledgments

This work was supported in part by the National Institutes of Health (NIDCR R01 DE029655, NIDCD, R01DC014461), National Science Foundation (NSF, DMR 2243648), and Delaware Bioscience Center for Advanced Technology (DE-CAT 12A00448). The authors also acknowledge the use of facilities and instrumentation supported by NSF through the University of Delaware Materials Research Science and Engineering Center (DMR 2011824). Microscopy access was supported by grants from the NIH-NIGMS (P20 GM103446), the NSF (IIA-1301765), and the State of Delaware. We thank Drs. Jeffrey Caplan and Sylvain Le Marchand for their expert assistance in confocal imaging and image analysis. We thank Sanofi/Genzyme for generously providing HA.

Data Availability

As part of an ongoing study, the raw/processed data required to reproduce these findings are available from the corresponding author on reasonable request.

References

- 1. Witt, R. L., Salivary gland diseases: surgical and medical management. Thieme: New York, 2005.
- 2. Harunaga, J. S.; Doyle, A. D.; Yamada, K. M., Local and global dynamics of the basement membrane during branching morphogenesis require protease activity and actomyosin contractility. *Dev Biol* **2014**, *394* (2), 197-205.
- 3. Manfrè, V.; Chatzis, L. G.; Cafaro, G.; Fonzetti, S.; Calvacchi, S.; Fulvio, G.; Navarro Garcia, I. C.; La Rocca, G.; Ferro, F.; Perricone, C.; Bartoloni, E.; Baldini, C., Sjögren's syndrome: one year in review 2022. *Clin Exp Rheumatol* **2022**, *40* (12), 2211-2224.
- 4. Fox, R. I.; Fox, C. M.; McCoy, S. S., Emerging treatment for Sjögren's disease: a review of recent phase II and III trials. *Expert Opin Emerg Drugs* **2023**, *28* (2), 107-120.
- 5. Yura, Y.; Hamada, M., Outline of Salivary Gland Pathogenesis of Sjögren's Syndrome and Current Therapeutic Approaches. *Int J Mol Sci* **2023**, *24* (13).
- 6. Sullivan, C. A.; Haddad, R. I.; Tishler, R. B.; Mahadevan, A.; Krane, J. F., Chemoradiation-induced cell loss in human submandibular glands. *Laryngoscope* **2005**, *115* (6), 958-64.
- 7. Dirix, P.; Nuyts, S.; Van den Bogaert, W., Radiation-induced xerostomia in patients with head and neck cancer: a literature review. *Cancer* **2006**, *107* (11), 2525-34.
- 8. Sasportas, L. S.; Hosford, D. N.; Sodini, M. A.; Waters, D. J.; Zambricki, E. A.; Barral, J. K.; Graves, E. E.; Brinton, T. J.; Yock, P. G.; Le, Q. T.; Sirjani, D., Cost-effectiveness landscape analysis of treatments addressing xerostomia in patients receiving head and neck radiation therapy. *Oral surgery, oral medicine, oral pathology and oral radiology* **2013**, *116* (1), e37-51.
- 9. Salum, F. G.; Medella-Junior, F. A. C.; Figueiredo, M. A. Z.; Cherubini, K., Salivary hypofunction: An update on therapeutic strategies. *Gerodontology* **2018**, *35* (4), 305-316.
- 10. Mercadante, V.; Al Hamad, A.; Lodi, G.; Porter, S.; Fedele, S., Interventions for the management of radiotherapy-induced xerostomia and hyposalivation: A systematic review and meta-analysis. *Oral oncology* **2017**, *66*, 64-74.
- 11. Ma, S. J.; Rivers, C. I.; Serra, L. M.; Singh, A. K., Long-term outcomes of interventions for radiation-induced xerostomia: A review. *World journal of clinical oncology* **2019**, *10* (1), 1-13.
- 12. Wang, J. H., D.; Yu, H.; Cheng, Y.; Ren, H.; Zhao, Y., Developing tissue engineering strategies for liver regeneration. *Engineered Regeneration* **2022**, *3*, 80-91.
- 13. Ozdemir, T.; Fowler, E. W.; Hao, Y.; Ravikrishnan, A.; Harrington, D. A.; Witt, R. L.; Farach-Carson, M. C.; Pradhan-Bhatt, S.; Jia, X., Biomaterials-based strategies for salivary gland tissue regeneration. *Biomaterials science* **2016**, *4* (4), 592-604.
- 14. Pradhan-Bhatt, S.; Harrington, D. A.; Duncan, R. L.; Jia, X.; Witt, R. L.; Farach-Carson, M. C., Implantable three-dimensional salivary spheroid assemblies demonstrate fluid and protein secretory responses to neurotransmitters. *Tissue engineering. Part A* **2013**, *19* (13-14), 1610-20.
- 15. Ozdemir, T.; Fowler, E. W.; Liu, S.; Harrington, D. A.; Witt, R. L.; Farach-Carson, M. C.; Pradhan-Bhatt, S.; Jia, X., Tuning Hydrogel Properties to Promote the Assembly of Salivary Gland Spheroids in 3D. *ACS Biomater Sci Eng* **2016**, *2* (12), 2217-2230.
- 16. Ozdemir, T.; Srinivasan, P. P.; Zakheim, D. R.; Harrington, D. A.; Witt, R. L.; Farach-Carson, M. C.; Jia, X.; Pradhan-Bhatt, S., Bottom-up assembly of salivary gland microtissues for assessing myoepithelial cell function. *Biomaterials* **2017**, *142*, 124-135.

- 17. Srinivasan, P. P.; Patel, V. N.; Liu, S.; Harrington, D. A.; Hoffman, M. P.; Jia, X.; Witt, R. L.; Farach-Carson, M. C.; Pradhan-Bhatt, S., Primary Salivary Human Stem/Progenitor Cells Undergo Microenvironment-Driven Acinar-Like Differentiation in Hyaluronate Hydrogel Culture. *Stem cells translational medicine* **2017**, *6* (1), 110-120.
- 18. Fowler, E. W.; Ravikrishnan, A.; Witt, R. L.; Pradhan-Bhatt, S.; Jia, X., RGDSP-Decorated Hyaluronate Hydrogels Facilitate Rapid 3D Expansion of Amylase-Expressing Salivary Gland Progenitor Cells. *ACS Biomater Sci Eng* **2021**, *7* (12), 5749-5761.
- 19. Fowler, E. W.; van Venrooy, E. J.; Witt, R. L.; Jia, X., A TGFβR inhibitor represses keratin-7 expression in 3D cultures of human salivary gland progenitor cells. *Sci Rep* **2022**, *12* (1), 15008.
- 20. Metkari, A. S.; Fowler, E. W.; Witt, R. L.; Jia, X., Matrix Degradability Contributes to the Development of Salivary Gland Progenitor Cells with Secretory Functions. *ACS Appl Mater Interfaces* **2023**, *15* (27), 32148-32161.
- 21. Sekiguchi, R.; Yamada, K. M., Basement Membranes in Development and Disease. *Curr Top Dev Biol* **2018**, *130*, 143-191.
- 22. Wang, S.; Matsumoto, K.; Lish, S. R.; Cartagena-Rivera, A. X.; Yamada, K. M., Budding epithelial morphogenesis driven by cell-matrix versus cell-cell adhesion. *Cell* **2021**, *184* (14), 3702-3716.e30.
- 23. Miner, J. H.; Yurchenco, P. D., Laminin functions in tissue morphogenesis. *Annual review of cell and developmental biology* **2004**, *20*, 255-84.
- 24. Kadoya, Y.; Yamashina, S., Salivary gland morphogenesis and basement membranes. *Anatomical science international* **2005**, *80* (2), 71-9.
- 25. Patel, V. N.; Pineda, D. L.; Hoffman, M. P., The function of heparan sulfate during branching morphogenesis. *Matrix Biol* **2017**, *57-58*, 311-323.
- 26. Thotakura, S.; Basova, L.; Makarenkova, H. P., FGF Gradient Controls Boundary Position Between Proliferating and Differentiating Cells and Regulates Lacrimal Gland Growth Dynamics. *Front Genet* **2019**, *10*, 362.
- 27. Chlasta, J.; Milani, P.; Runel, G.; Duteyrat, J. L.; Arias, L.; Lamire, L. A.; Boudaoud, A.; Grammont, M., Variations in basement membrane mechanics are linked to epithelial morphogenesis. *Development* **2017**, *144* (23), 4350-4362.
- 28. Voit, B. I.; Lederer, A., Hyperbranched and highly branched polymer architectures-synthetic strategies and major characterization aspects. *Chem Rev* **2009**, *109* (11), 5924-73.
- 29. Anilkumar, P.; Lawson, T. B.; Abbina, S.; Makela, J. T. A.; Sabatelle, R. C.; Takeuchi, L. E.; Snyder, B. D.; Grinstaff, M. W.; Kizhakkedathu, J. N., Mega macromolecules as single molecule lubricants for hard and soft surfaces. *Nat Commun* **2020**, *11* (1), 2139.
- 30. ul-Haq, M. I.; Shenoi, R. A.; Brooks, D. E.; Kizhakkedathu, J. N., Solvent-assisted anionic ring opening polymerization of glycidol: Toward medium and high molecular weight hyperbranched polyglycerols. *Journal of Polymer Science Part a-Polymer Chemistry* **2013**, *51* (12), 2614-2621.
- 31. Pedron, S.; Pritchard, A. M.; Vincil, G. A.; Andrade, B.; Zimmerman, S. C.; Harley, B. A., Patterning Three-Dimensional Hydrogel Microenvironments Using Hyperbranched Polyglycerols for Independent Control of Mesh Size and Stiffness. *Biomacromolecules* **2017**, *18* (4), 1393-1400.
- 32. Gosecki, M.; Kazmierski, S.; Gosecka, M., Diffusion-Controllable Biomineralization Conducted In Situ in Hydrogels Based on Reversibly Cross-Linked Hyperbranched Polyglycidol. *Biomacromolecules* **2017**, *18* (10), 3418-3431.

- 33. Wu, C.; Strehmel, C.; Achazi, K.; Chiappisi, L.; Dernedde, J.; Lensen, M. C.; Gradzielski, M.; Ansorge-Schumacher, M. B.; Haag, R., Enzymatically cross-linked hyperbranched polyglycerol hydrogels as scaffolds for living cells. *Biomacromolecules* **2014**, *15* (11), 3881-90.
- 34. Zhang, H.; Patel, A.; Gaharwar, A. K.; Mihaila, S. M.; Iviglia, G.; Mukundan, S.; Bae, H.; Yang, H.; Khademhosseini, A., Hyperbranched polyester hydrogels with controlled drug release and cell adhesion properties. *Biomacromolecules* **2013**, *14* (5), 1299-310.
- 35. Steinhilber, D.; Seiffert, S.; Heyman, J. A.; Paulus, F.; Weitz, D. A.; Haag, R., Hyperbranched polyglycerols on the nanometer and micrometer scale. *Biomaterials* **2011**, *32* (5), 1311-6.
- 36. Zhang, H.; Zhao, C.; Cao, H.; Wang, G.; Song, L.; Niu, G.; Yang, H.; Ma, J.; Zhu, S., Hyperbranched poly(amine-ester) based hydrogels for controlled multi-drug release in combination chemotherapy. *Biomaterials* **2010**, *31* (20), 5445-54.
- 37. Oudshoorn, M. H.; Penterman, R.; Rissmann, R.; Bouwstra, J. A.; Broer, D. J.; Hennink, W. E., Preparation and characterization of structured hydrogel microparticles based on cross-linked hyperbranched polyglycerol. *Langmuir* **2007**, *23* (23), 11819-25.
- 38. Hong, J.; Shin, Y.; Kim, S.; Lee, J.; Cha, C., Complex Tuning of Physical Properties of Hyperbranched Polyglycerol-Based Bioink for Microfabrication of Cell-Laden Hydrogels. *Advanced Functional Materials* **2019**, *29* (13), 1808750.
- 39. Dey, P.; Schneider, T.; Chiappisi, L.; Gradzielski, M.; Schulze-Tanzil, G.; Haag, R., Mimicking of Chondrocyte Microenvironment Using In Situ Forming Dendritic Polyglycerol Sulfate-Based Synthetic Polyanionic Hydrogels. *Macromol Biosci* **2016**, *16* (4), 580-90.
- 40. Pedron, S.; Peinado, C.; Bosch, P.; Anseth, K. S., Synthesis and characterization of degradable bioconjugated hydrogels with hyperbranched multifunctional cross-linkers. *Acta Biomater* **2010**, *6* (11), 4189-98.
- 41. Dong, Y.; Hassan, W. U.; Kennedy, R.; Greiser, U.; Pandit, A.; Garcia, Y.; Wang, W., Performance of an in situ formed bioactive hydrogel dressing from a PEG-based hyperbranched multifunctional copolymer. *Acta Biomater* **2014**, *10* (5), 2076-85.
- 42. Dong, Y. X.; Sigen, A.; Rodrigues, M.; Li, X. L.; Kwon, S. H.; Kosaric, N.; Khong, S.; Gao, Y. S.; Wang, W. X.; Gurtner, G. C., Injectable and Tunable Gelatin Hydrogels Enhance Stem Cell Retention and Improve Cutaneous Wound Healing. *Advanced Functional Materials* **2017**, *27* (24).
- 43. Kennedy, R.; Ul Hassan, W.; Tochwin, A.; Zhao, T. Y.; Dong, Y. X.; Wang, Q.; Tai, H. Y.; Wang, W. X., In situ formed hybrid hydrogels from PEG based multifunctional hyperbranched copolymers: a RAFT approach. *Polymer Chemistry* **2014**, *5* (6), 1838-1842.
- 44. Liu, M.; Mao, X.-a.; Ye, C.; Huang, H.; Nicholson, J. K.; Lindon, J. C., Improved WATERGATE Pulse Sequences for Solvent Suppression in NMR Spectroscopy. *Journal of Magnetic Resonance* **1998**, *132*, 125-129.
- 45. Haslauer, K. E.; Hemmler, D.; Schmitt-Kopplin, P.; Heinzmann, S. S., Guidelines for the Use of Deuterium Oxide (D(2)O) in (1)H NMR Metabolomics. *Anal Chem* **2019**, *91* (17), 11063-11069.
- 46. Kainthan, R. K.; Muliawan, E. B.; Hatzikiriakos, S. G.; Brooks, D. E., Synthesis, Characterization, and Viscoelastic Properties of High Molecular Weight Hyperbranched Polyglycerols. *Macromolecules* **2006**, *39* (22), 7708-7717.

- 47. Frazier, S. B.; Roodhouse, K. A.; Hourcade, D. E.; Zhang, L., The Quantification of Glycosaminoglycans: A Comparison of HPLC, Carbazole, and Alcian Blue Methods. *Open Glycosci* **2008**, *1*, 31-39.
- 48. Soumpasis, D. M., Theoretical analysis of fluorescence photobleaching recovery experiments. *Biophys J* **1983**, *41* (1), 95-7.
- 49. Branco, M. C.; Pochan, D. J.; Wagner, N. J.; Schneider, J. P., Macromolecular diffusion and release from self-assembled beta-hairpin peptide hydrogels. *Biomaterials* **2009**, *30* (7), 1339-47.
- 50. Armstrong, J. K.; Wenby, R. B.; Meiselman, H. J.; Fisher, T. C., The hydrodynamic radii of macromolecules and their effect on red blood cell aggregation. *Biophys J* **2004**, *87* (6), 4259-70.
- 51. Bernhard, S. P.; Fricke, M. S.; Haag, R.; Cloninger, M. J., Protein Aggregation Nucleated by Functionalized Dendritic Polyglycerols. *Polym Chem* **2020**, *11* (23), 3849-3862.
- 52. Burakowska, E.; Quinn, J. R.; Zimmerman, S. C.; Haag, R., Cross-linked hyperbranched polyglycerols as hosts for selective binding of guest molecules. *J Am Chem Soc* **2009**, *131* (30), 10574-80.
- 53. Kainthan, R. K.; Janzen, J.; Kizhakkedathu, J. N.; Devine, D. V.; Brooks, D. E., Hydrophobically derivatized hyperbranched polyglycerol as a human serum albumin substitute. *Biomaterials* **2008**, *29* (11), 1693-704.
- 54. Purcell, B. P.; Kim, I. L.; Chuo, V.; Guinen, T.; Dorsey, S. M.; Burdick, J. A., Incorporation of Sulfated Hyaluronic Acid Macromers into Degradable Hydrogel Scaffolds for Sustained Molecule Delivery. *Biomaterials science* **2014**, *2*, 693-702.
- 55. Weinhart, M.; Becherer, T.; Schnurbusch, N.; Schwibbert, K.; Kunte, H.-J.; Haag, R., Linear and Hyperbranched Polyglycerol Derivatives as Excellent Bioinert Glass Coating Materials. *Advanced Engineering Materials* **2011**, *13* (12), B501-B510.
- 56. Burzava, A. L. S.; Jasieniak, M.; Cockshell, M. P.; Voelcker, N. H.; Bonder, C. S.; Griesser, H. J.; Moore, E., Surface-Grafted Hyperbranched Polyglycerol Coating: Varying Extents of Fouling Resistance across a Range of Proteins and Cells. *ACS Appl Bio Mater* **2020**, *3* (6), 3718-3730.
- 57. Patel, V. N.; Hoffman, M. P., Salivary gland development: a template for regeneration. *Semin Cell Dev Biol* **2014**, *25-26*, 52-60.
- 58. Li, Y.; Sun, C.; Yates, E. A.; Jiang, C.; Wilkinson, M. C.; Fernig, D. G., Heparin binding preference and structures in the fibroblast growth factor family parallel their evolutionary diversification. *Open Biol* **2016**, *6* (3).
- 59. Buchtova, M.; Chaloupkova, R.; Zakrzewska, M.; Vesela, I.; Cela, P.; Barathova, J.; Gudernova, I.; Zajickova, R.; Trantirek, L.; Martin, J.; Kostas, M.; Otlewski, J.; Damborsky, J.; Kozubik, A.; Wiedlocha, A.; Krejci, P., Instability restricts signaling of multiple fibroblast growth factors. *Cell Mol Life Sci* **2015**, *72* (12), 2445-59.
- 60. Daley, W. P.; Kohn, J. M.; Larsen, M., A focal adhesion protein-based mechanochemical checkpoint regulates cleft progression during branching morphogenesis. *Dev Dyn* **2011**, *240* (9), 2069-83.
- 61. Daley, W. P.; Gervais, E. M.; Centanni, S. W.; Gulfo, K. M.; Nelson, D. A.; Larsen, M., ROCK1-directed basement membrane positioning coordinates epithelial tissue polarity. *Development* **2012**, *139* (2), 411-22.
- 62. Koslow, M.; O'Keefe, K. J.; Hosseini, Z. F.; Nelson, D. A.; Larsen, M., ROCK inhibitor increases proacinar cells in adult salivary gland organoids. *Stem Cell Res* **2019**, *41*, 101608.

- 63. Grandy, C.; Port, F.; Pfeil, J.; Gottschalk, K. E., Influence of ROCK Pathway Manipulation on the Actin Cytoskeleton Height. *Cells* **2022**, *11* (3).
- 64. Ambudkar, I. S., Polarization of calcium signaling and fluid secretion in salivary gland cells. *Curr Med Chem* **2012**, *19* (34), 5774-81.
- 65. Cantara, S. I.; Soscia, D. A.; Sequeira, S. J.; Jean-Gilles, R. P.; Castracane, J.; Larsen, M., Selective functionalization of nanofiber scaffolds to regulate salivary gland epithelial cell proliferation and polarity. *Biomaterials* **2012**, *33* (33), 8372-82.
- 66. Martin-Belmonte, F.; Gassama, A.; Datta, A.; Yu, W.; Rescher, U.; Gerke, V.; Mostov, K., PTEN-mediated apical segregation of phosphoinositides controls epithelial morphogenesis through Cdc42. *Cell* **2007**, *128* (2), 383-97.
- 67. Grikscheit, K.; Grosse, R., Formins at the Junction. *Trends Biochem Sci* **2016**, *41* (2), 148-159.
- 68. Co, J. Y.; Margalef-Català, M.; Monack, D. M.; Amieva, M. R., Controlling the polarity of human gastrointestinal organoids to investigate epithelial biology and infectious diseases. *Nat Protoc* **2021**, *16* (11), 5171-5192.
- 69. Søgaard, P. P.; Ito, N.; Sato, N.; Fujita, Y.; Matter, K.; Itoh, Y., Epithelial polarization in 3D matrix requires DDR1 signaling to regulate actomyosin contractility. *Life Sci Alliance* **2019**, 2 (1).
- 70. Ivanov, A. I.; Hopkins, A. M.; Brown, G. T.; Gerner-Smidt, K.; Babbin, B. A.; Parkos, C. A.; Nusrat, A., Myosin II regulates the shape of three-dimensional intestinal epithelial cysts. *J Cell Sci* **2008**, *121* (11), 1803-14.
- 71. Libanje, F.; Raingeaud, J.; Luan, R.; Thomas, Z.; Zajac, O.; Veiga, J.; Marisa, L.; Adam, J.; Boige, V.; Malka, D.; Goere, D.; Hall, A.; Soazec, J. Y.; Prall, F.; Gelli, M.; Dartigues, P.; Jaulin, F., ROCK2 inhibition triggers the collective invasion of colorectal adenocarcinomas. *EMBO J* **2019**, *38* (14), e99299.
- 72. Emmerson, E.; May, A. J.; Berthoin, L.; Cruz-Pacheco, N.; Nathan, S.; Mattingly, A. J.; Chang, J. L.; Ryan, W. R.; Tward, A. D.; Knox, S. M., Salivary glands regenerate after radiation injury through SOX2-mediated secretory cell replacement. *EMBO Mol Med* **2018**, *10* (3).
- 73. Min, S.; Oyelakin, A.; Gluck, C.; Bard, J. E.; Song, E. C.; Smalley, K.; Che, M.; Flores, E.; Sinha, S.; Romano, R. A., p63 and Its Target Follistatin Maintain Salivary Gland Stem/Progenitor Cell Function through TGF-beta/Activin Signaling. *iScience* **2020**, *23* (9), 101524.
- 74. Suzuki, D.; Pinto, F.; Senoo, M., Inhibition of TGF-beta signaling supports high proliferative potential of diverse p63(+) mouse epithelial progenitor cells in vitro. *Sci Rep* **2017**, 7 (1), 6089.

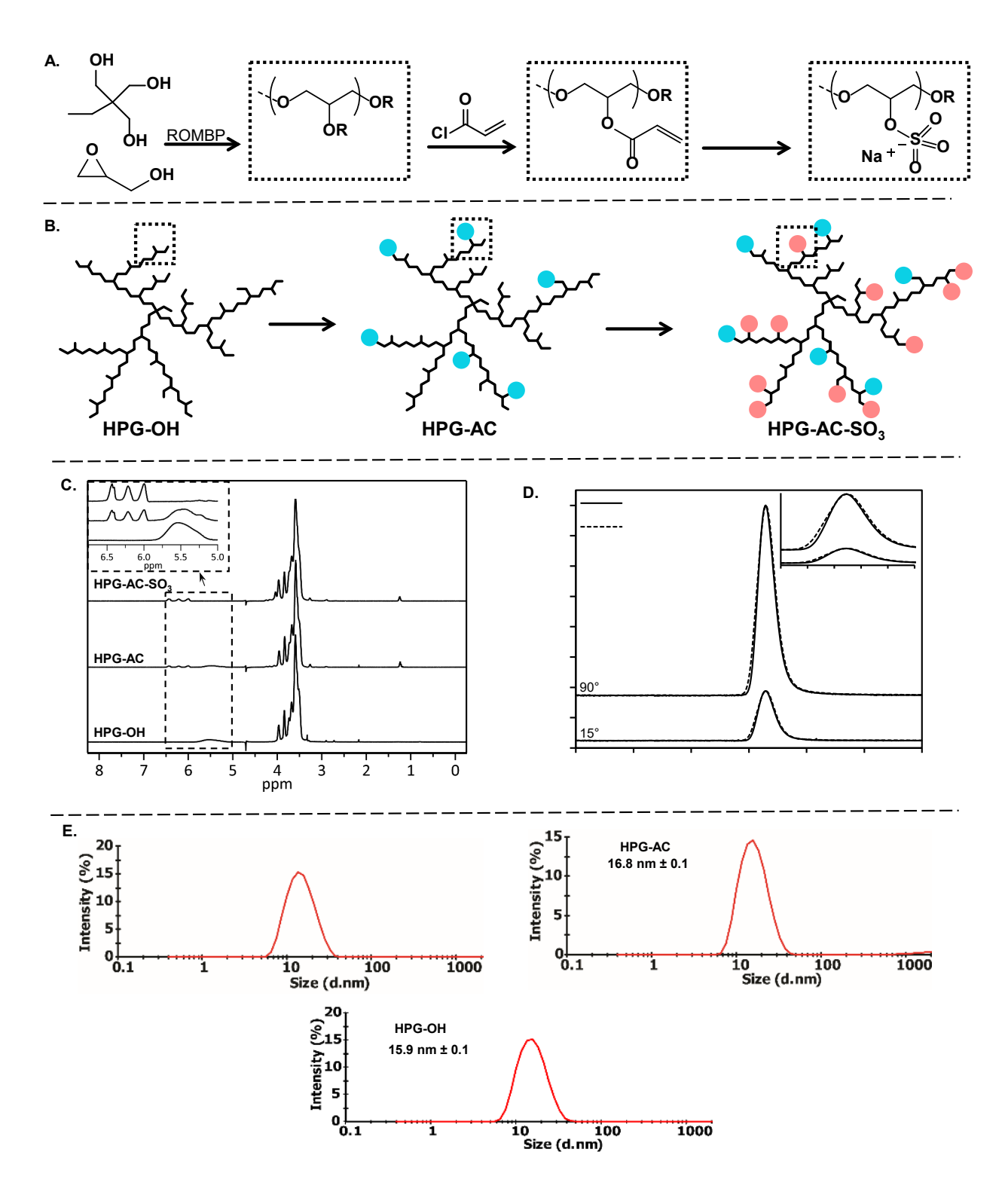


Figure 1. Synthesis and characterization of hyperbranched polyglycerol (HPG) derivatives. (A) High molecular weight HPG-OH were synthesized from glycidol and trimethylolpropane (TMP) via ROMBP with an emulsifying agent (dioxane). R = -H / -CH₂-. Esterification of the hydroxyl groups with acryloyl chloride produced HPG-AC. R = -H / -CH₂-/ -COCH=CH₂. Sulfation of hydroxyl groups in HPG-AC with a DMF-SO₃ yielded HPG-AC-SO₃. R = -H / -CH₂-/ -COCHCH₂ / -SO₃Na. (B) Idealized structures of HPG derivatives. Boxed region indicates the location of functional groups shown in (A). Acrylate and sulfate groups are represented as cyan and magenta spheres, respectively. Randomly distributed hydroxyls are not shown. (C) ¹H-NMR spectra showing the presence of glycidol backbone protons at 3.2-4.2 ppm, hydroxyl protons at 5.0-5.75 ppm and the vinyl protons at 6.0-6.5 ppm. Insert shows the expanded region at 5.0-6.75 ppm. i: HPG-OH, ii: HPG-AC, iii: HPG-AC-SO₃. (D) Gel permeation chromatograph (GPC) of HPG-OH and HPG-AC acquired with a multiangle laser light scattering (MALLS) detector using an aqueous mobile phase with 0.1 M NaNO₃. Insert shows the expanded region at 14-19 min. (E) Characterization of the hydrodynamic diameter of HPG derivatives by dynamic light scattering (DLS).

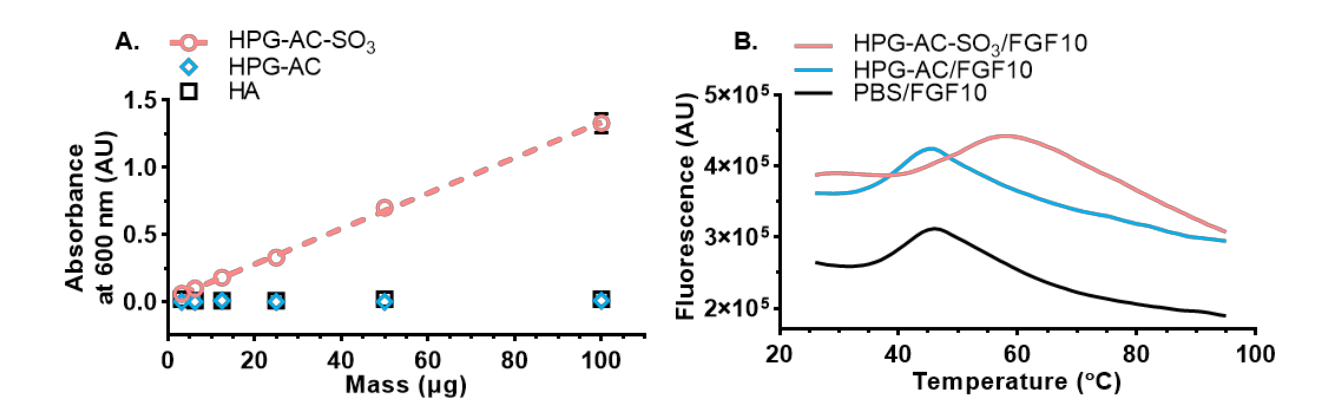


Figure 2. Characterization of HPG-AC-SO₃. **(A)** Alcian blue assay confirming the presence of sulfate groups. A linear response curve was constructed by coating the plate with 3.1 to 100 μ g HPG-AC-SO₃. Open symbols represent the experimental data, and the dashed line represents a linear regression (R² = 0.999). Alcain blue assay conducted with the HPG-AC and HA controls does not show any absorbance at 600 nm. **(B)** DSF analysis of FGF10 stability in the presence of HPG-AC-SO₃, HPG-AC and PBS. Sypro Orange dye was used to detect protein unfolding.

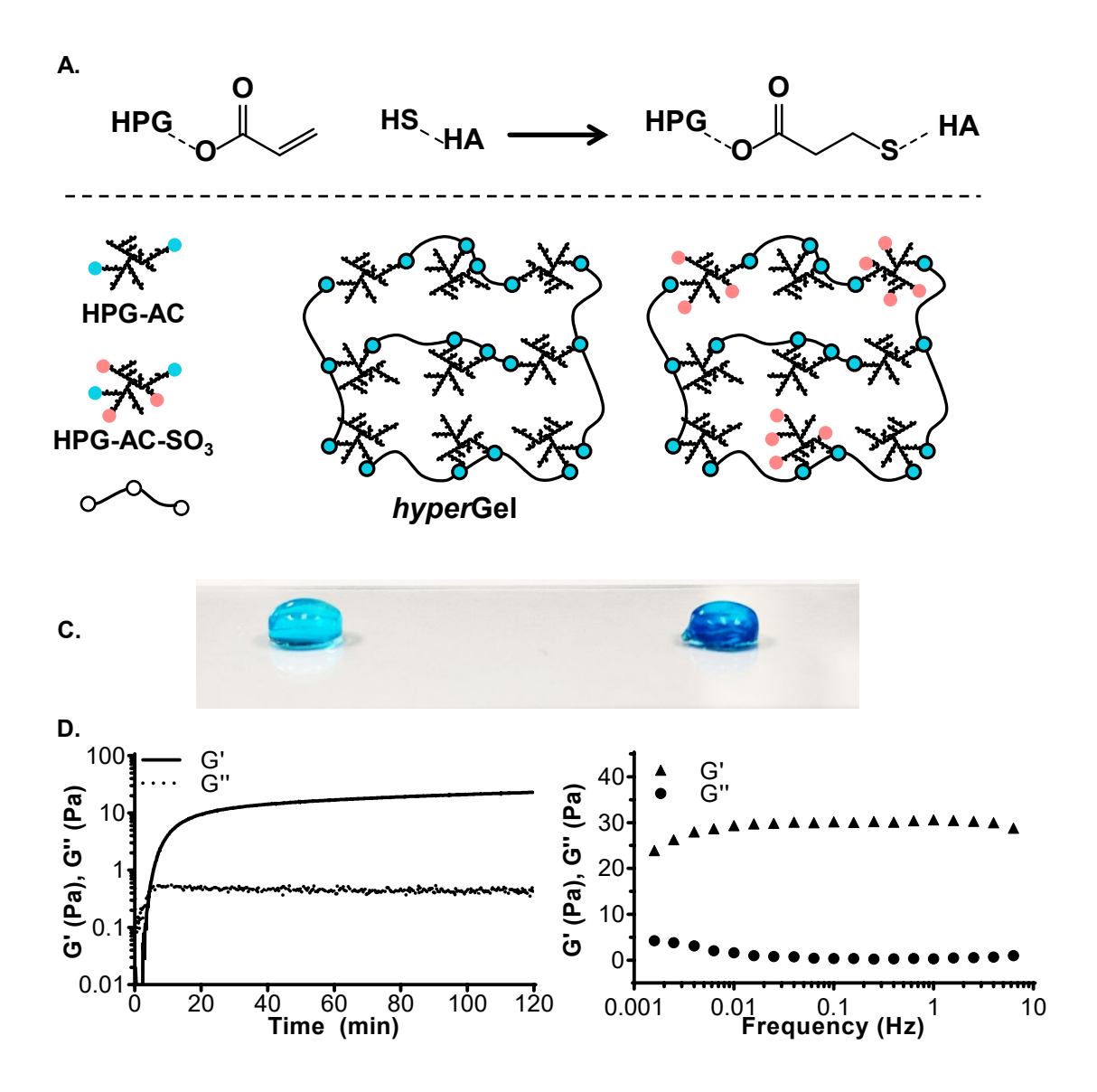


Figure 3. Characterization of hyperGel and hyperGel+ by Alcian blue staining and oscillatory shear rheology. **(A)** Hydrogels were produced via Michael-type addition reaction between the sulfhydryl groups in HA and the acrylate groups in HPG. **(B)** hperGels were prepared using the HA-SH and HPG-AC. Sulfated hyperGels (hyperGel+) were prepared using HA-SH and HPG-AC / HPG-AC-SO₃ solutions (1% in PBS+) at a volume ratio of 1/20. **(C)** Digital pictures of Alcian blue stained hyperGels. The intense blue color observed from hyperGel+ confirmed the incorporation of sulfate groups in the hydrogel. **(D)** The viscoelastic properties of the hyperGel were analysed with parallel plate rheology. Left: time sweep; Right: Frequency sweep.

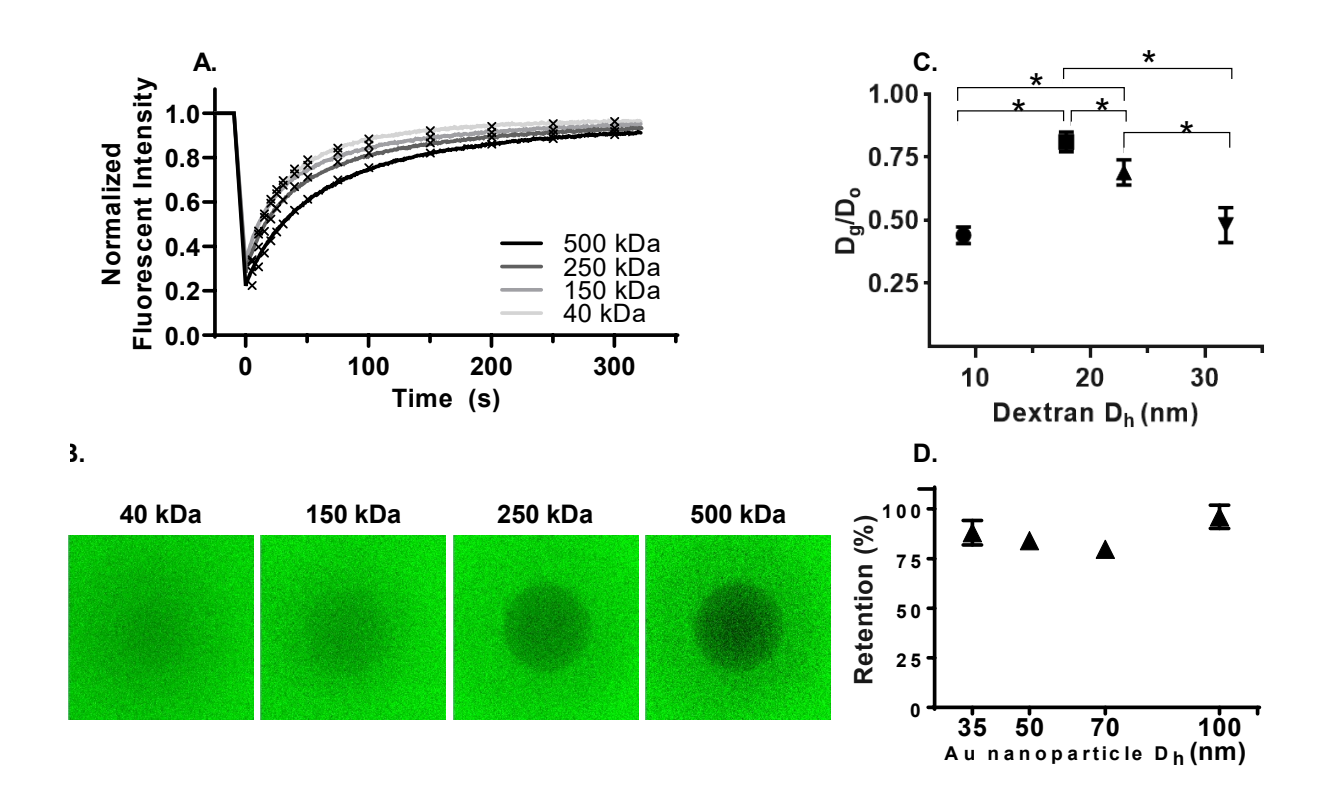


Figure 4. Analysis of hydrogel pore size by FRAP (A-C) and nanoparticle retention (D). (A) Normalized FRAP signals for 40, 150, 250, and 500 kDa FITC-dextran in hyperGel equilibrated in PBS. (B) Confocal microscopy images of hyperGels containing 40, 150, 250, and 500 kDa FITC-dextran 40 s post bleaching. (C) Normalized diffusion coefficient as a function of probe size. Dg: diffusion coefficient of FITC-dextran in the hyperGel. D₀: diffusion coefficient of FITC-dextran in PBS. The diameter of hydration was 8.94, 17.90, 22.92 and 31.80 nm for FITC-dextran with a molecular weight of 40 kDa (●), 150 kDa (■), 250 kDa (▲) and 500 kDa (▼), respectively. (D) Estimation of bulk hydrogel porosity using a nanoparticle retention assay. For quantitative analyses, two-way ANOVA was performed, followed by Tukey's multiple comparison test. Asterisk indicates significantly different (p < 0.05).

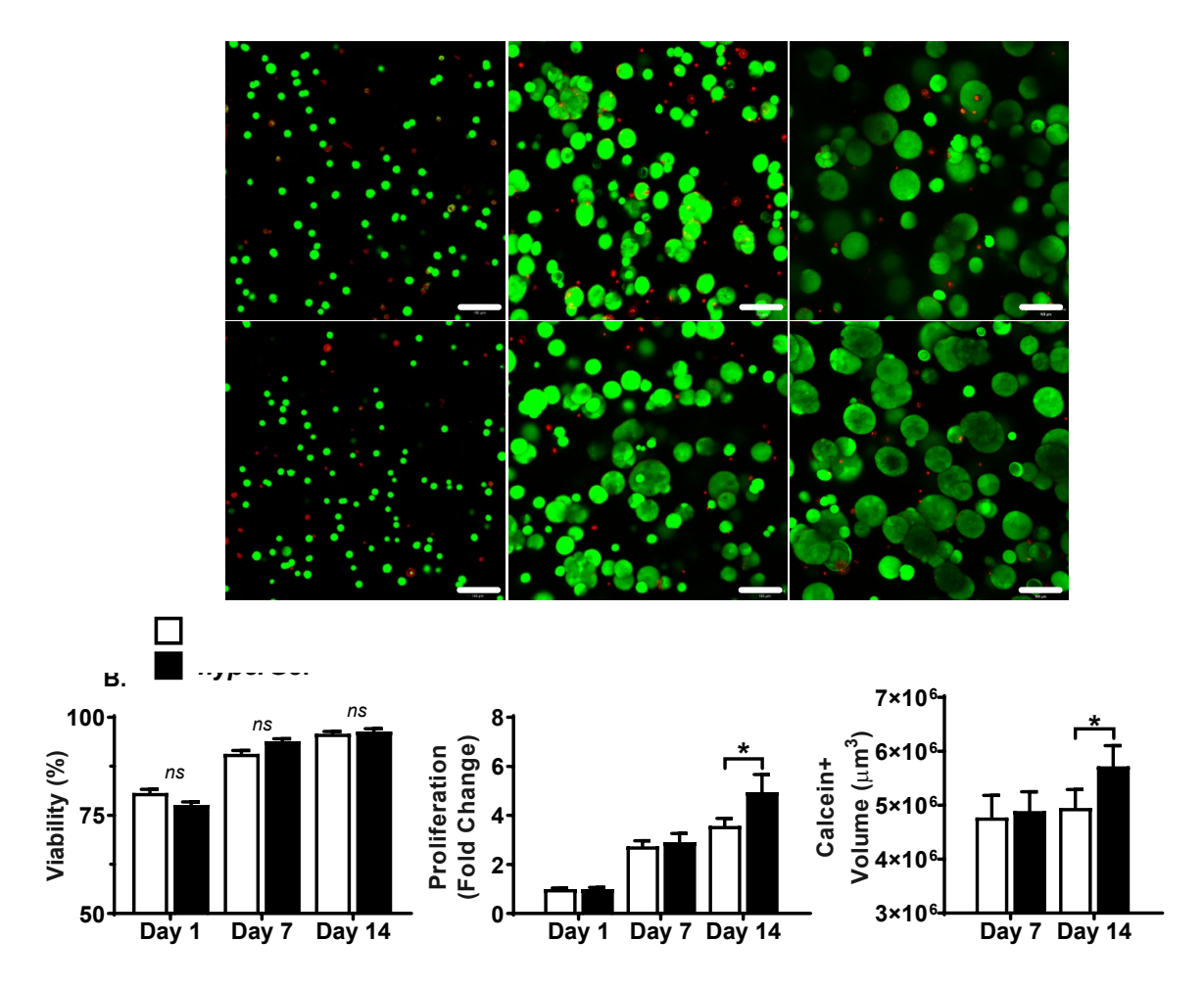


Figure 5. Cytocompatible hyperGel and hyperGel+ stimulate the 3D expansion and organized growth of hS/PCs. **(A)** Representative confocal images of hS/PCs with live/dead staining. Live cells were stained green by Calcein-AM and dead cells were stained red by EthD-1. Scale bar: 100 μ m. **(B-C)** Viability (B) and proliferation (C) were quantified from Hoechst 33324 (Figure S7) and EthD-1-stained nuclei. **(D)** 3D reconstruction was performed on calcein-stained spheroids to determine the average spheroid volume. Error bars represent SEM. For quantitative analyses, two-way ANOVA was performed, followed by a post hoc Tukey's test. Asterisk indicates significantly different (p < 0.05).

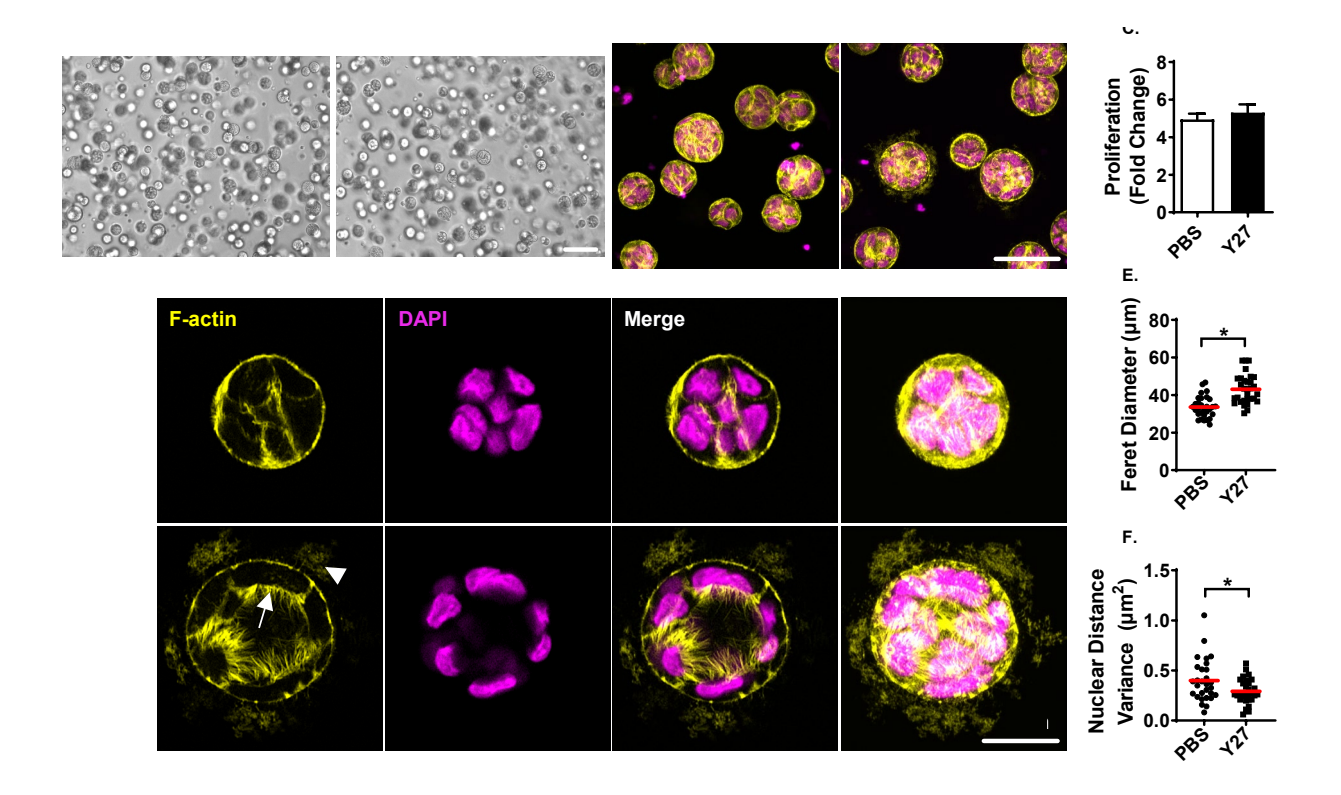


Figure 6. ROCK inhibition led to the development of hS/PC spheroids with a central lumen and F-actin rich protrusions. (A) hS/PCs were cultured in the hyperGel+ for 14 days in medium supplemented with Y27 or the vehicle control, PBS, and visualized with brightfield microscopy. (B) After 14 days of culture in hyperGel+ with Y27, constructs were fixed, stained, and visualized with confocal microscopy. DAPI: Magenta, F-actin: yellow. (C) Cell proliferation was determined by enumerating DAPI stained nuclei from confocal microscopy images. (D) High magnification confocal images showing the morphology of representative spheroids developed in hyperGels+. DAPI: Magenta, F-actin: yellow. MIP: maximum intensity projection. White arrow and arrowhead point to F-actin-rich structures extending into the lumen and the gel, respectively. (E) Spheroid Feret diameter was determined from maximum intensity projections of confocal images shown in (C) using ImageJ. (F) 3D reconstructions of images shown in (C) were prepared in Imaris to determine the variance in the distance of individual nuclei from the spheroid centroid. For quantitative analyses, student's t-tests were performed. Asterisk indicates significantly different, p < 0.05.

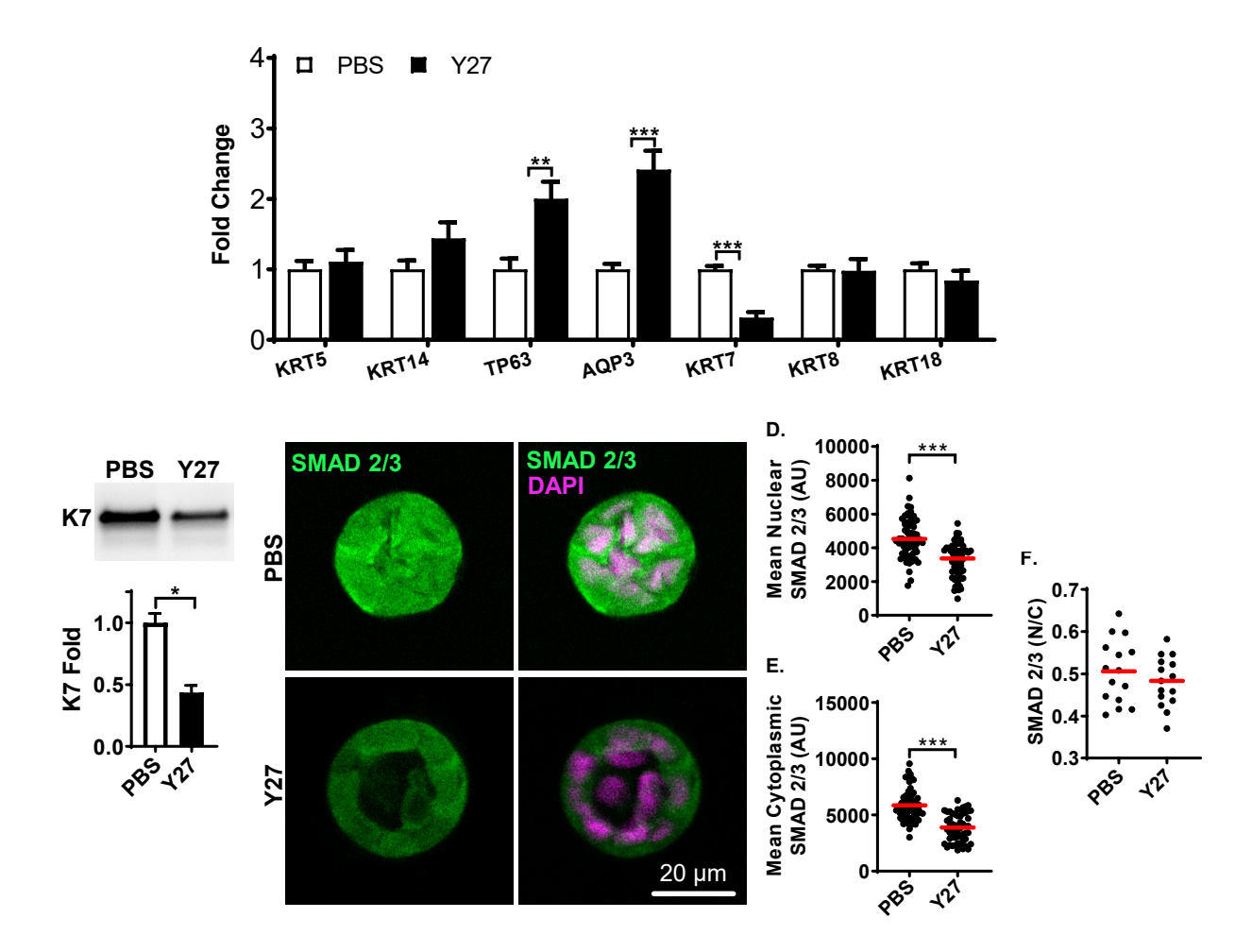


Figure 7. ROCK inhibition increased the expression of AQP3, decreased the expression of KRT7/K7 and attenuated TGF-β signaling. **(A)** Expression of stem, progenitor, acinar, and ductal markers at the mRNA level by qPCR. **(B)** K7 expression determined by Western blotting. **(C)** Characterization of SMAD2/3 expression (green) by immunohistochemistry. Images were acquired using Zeiss LSM 880. Nuclei were counterstained by DAPI (magenta). **(D-F)** 3D reconstruction of confocal images after SMAD 2/3 and DAPI staining was prepared in Imaris to determine the mean SMAD 2/3 nuclear intensity (D), mean cytoplasmic SMAD2/3 intensity (E), and SMAD 2/3 nuclear/cytoplasmic (N/C) ratio (F). For quantitative analyses, Student's t-tests were performed. Asterisk indicates significantly different. *: p < 0.05, **: p < 0.002, ***: p < 0.001.